doi:10.1016/j.jmb.2010.09.012 J. Mol. Biol. (2010) 403, 591–606

Contents lists available at www.sciencedirect.com

Journal of Molecular Biology

journal homepage: http://ees.elsevier.com.jmb

Solution Structure and Phospholipid Interactions of the Isolated Voltage-Sensor Domain from KvAP

Joel A. Butterwick* and Roderick MacKinnon*

Howard Hughes Medical Institute and the Laboratory of Molecular Neurobiology and Biophysics, The Rockefeller University, 1230 York Avenue, New York, NY 10065, USA

Received 26 May 2010; received in revised form 4 September 2010; accepted 7 September 2010
Available online 21 September 2010

Edited by J. Bowie

Keywords:
NMR spectroscopy; ion channel; protein–lipid interactions; membrane protein structure; membrane protein dynamics

Voltage-sensor domains (VSDs) are specialized transmembrane segments that confer voltage sensitivity to many proteins such as ion channels and enzymes. The activities of these domains are highly dependent on both the chemical properties and the physical properties of the surrounding membrane environment. To learn about VSD–lipid interactions, we used nuclear magnetic resonance spectroscopy to determine the structure and phospholipid interface of the VSD from the voltage-dependent K^+ channel KvAP (prokaryotic Kv from *Aeropyrum pernix*). The solution structure of the KvAP VSD solubilized within phospholipid micelles is similar to a previously determined crystal structure solubilized by a nonionic detergent and complexed with an antibody fragment. The differences observed include a previously unidentified short amphipathic α-helix that precedes the first transmembrane helix and a subtle rigid-body repositioning of the S3–S4 voltage-sensor paddle. Using ^{15}N relaxation experiments, we show that much of the VSD, including the pronounced kink in S3 and the S3–S4 paddle, is relatively rigid on the picosecond-to-nanosecond timescale. In contrast, the kink in S3 is mobile on the microsecond-to-millisecond timescale and may act as a hinge in the movement of the paddle during channel gating. We characterized the VSD–phospholipid micelle interactions using nuclear Overhauser effect spectroscopy and showed that the micelle uniformly coats the KvAP VSD and approximates the chemical environment of a phospholipid bilayer. Using paramagnetically labeled phospholipids, we show that bilayer-forming lipids interact with the S3 and S4 helices more strongly than with S1 and S2.

Introduction

Voltage-sensor domains (VSDs) are one of the principal molecular devices used to detect electrical potentials across lipid bilayers. These domains are characterized by a periodic set of positively charged residues (usually Arg) that move in response to changes in membrane electrical potential. Movement of these "gating charges" can be used to arbitrate proton permeation pathways within the VSD itself,[1–4] drive the opening and closing (gating) of coupled ion-conducting pore domains,[5] or modulate the activity of linked enzyme domains.[6]

*Corresponding authors. E-mail addresses: jbutterwic@rockefeller.edu; mackinn@rockefeller.edu.

Abbreviations used: VSD, voltage-sensor domain; DPC, *n*-dodecylphosphocholine; LDAO, lauryldimethylamine-*N*-oxide; HSQC, heteronuclear single-quantum coherence; D7PC, 1,2-diheptanoyl-*sn*-glycerol-3-phosphocholine; TROSY, transverse relaxation optimized spectroscopy; NOESY, nuclear Overhauser effect spectroscopy; NOE, nuclear Overhauser effect; hetNOE, heteronuclear nuclear Overhauser enhancement; PSPC, 1-palmitoyl-2-stearoyl-*sn*-glycero-3-phosphocholine; 3D, three-dimensional; 2D, two-dimensional; NIH, National Institutes of Health.

The crystal structures of voltage-dependent potassium-selective (Kv) channels consist of four VSDs that surround a central ion-conducting pore.[7–10] Independent movements of the VSDs synergistically act to gate the channel.[11] The overall structures of the VSDs are well conserved and consist of four transmembrane segments, termed S1–S4, with the gating charges located along S4. These domains appear largely exposed to the membrane, and their function is highly dependent on the chemical and physical properties of the lipid environment.[12–15] The charged phosphate group is especially important, as membranes devoid of phospholipids cannot support Kv channel function.[14,15] Furthermore, tarantula toxins that are known to partition into the membrane[16] interact with this domain and influence channel activity.[17,18]

Despite the growing appreciation for the importance of protein–lipid interactions, there is still much to be learned. The crystal structure of the eukaryotic Kv1.2–Kv2.1 "paddle chimera" contains a bilayer-like arrangement of cocrystallized lipids between the VSDs and the pore and between adjacent VSDs, but lipids are largely absent over the entire outer perimeter.[10] Lipid molecules are critical for correct channel conformation, as crystal structures determined in the absence of lipids contain distortions within the VSDs.[7,8] The exposure of KvAP (a prokaryotic Kv from *Aeropyrum pernix*) and its isolated VSD to membrane lipids has been inferred from electron paramagnetic resonance spectroscopy using conjugated nitroxide probes.[19,20] Four transmembrane helices were clearly identified; however, these experiments suffer from poor spatial resolution due to the long tether of the attached probes (~7 Å), and their interpretation rests on the assumption that the mutated residues do not affect the protein structure.

Here, we used nuclear magnetic resonance (NMR) spectroscopy to characterize the solution structure and dynamics of the isolated KvAP VSD encapsulated in a phospholipid micelle. Using this structure as the basis for further analyses, we were able to provide an atomic-resolution description of the aqueous, hydrophilic, and hydrophobic boundaries of the micelle and found that the phospholipid micelle approximates the chemical environment of a phospholipid bilayer. Next, we further characterized the association of bilayer-forming phospholipids using paramagnetically labeled compounds and showed that long-chain lipids preferentially interact with the S3 and S4 helices of the VSD. A recent study investigated the secondary structure and dynamics of the KvAP VSD solubilized in a mixture of the detergents *n*-dodecylphosphocholine (DPC) and lauryldimethylamine-*N*-oxide (LDAO).[21] Our results on secondary structure and dynamics are in overall agreement with that work.

Results

Solution NMR structure of the KvAP VSD

Initially, we sought to identify conditions suitable for NMR spectroscopy by recording ^{1}H–^{15}N heteronuclear single-quantum coherence (HSQC) spectra at 25 °C on uniformly ^{15}N-labeled (^{15}N) KvAP VSD solubilized in a variety of detergents. Gel-filtration chromatograms suggest that the KvAP VSD is relatively stable and monodisperse in many detergents; however, NMR spectra in these detergents showed a wide range of appearances, as judged by both the number and the dispersion of observed peaks (Fig. S1). The maltosides and glucosides, in particular, exhibited poor spectral dispersion and many fewer peaks than expected. In an earlier work,[7] this protein was extracted from *Escherichia coli* membranes using *n*-decyl-β-D-maltoside and crystallized in *n*-octyl-β-D-glucoside, suggesting that poor spectral quality in these detergents was not likely due to an inconvenient property of the protein (aggregation or conformational heterogeneity) but due to some property of the detergent micelle or protein–detergent interactions. One of the most promising detergents, the short-chain phospholipid 1,2-diheptanoyl-*sn*-glycerol-3-phosphocholine (D7PC), enabled high-quality spectra, and the KvAP VSD had been stable, even at 45 °C, for approximately 1 week before a significant loss of signal intensity began to occur. The higher temperature was chosen for further experiments because additional peaks were observed in ^{1}H–^{15}N HSQC spectra compared to 25 °C.

Resonance assignments for backbone ($^{1}H^{N}$, ^{15}N, $^{13}C'$, and $^{13}C^{\alpha}$) and $^{13}C^{\beta}$ nuclei at 45 °C and neutral pH were identified using transverse relaxation optimized spectroscopy (TROSY) HNCA, HNCO, HN(CO)CA, and HNCACB, and ^{15}N-edited ^{1}H–^{1}H nuclear Overhauser effect spectroscopy (NOESY) experiments[22] recorded using deuterated KvAP VSD samples (see Materials and Methods). These spectra permitted the assignment of approximately 65% of the backbone nuclei. To resolve ambiguities, we recorded HSQC, HNCA, and HNCO experiments on samples with different combinations of labeled amino acids so that specific amino acids and amino acid pairs could be distinguished in crowded regions of the spectra: (1) ^{13}C,^{15}N Arg; (2) ^{15}N Ile, 1-^{13}C Val, 2-^{13}C Leu; and (3) 1-^{13}C,^{15}N Leu, 2-^{13}C Gly, 2,3-^{13}C Ala. Resonance assignments were extended along the side chains using HC(C)H-COSY, and ^{13}C-edited and ^{15}N-edited NOESY experiments. Most ambiguities present among the methyl resonances were resolved by repeating the ^{13}C-edited NOESY using methyl-specific labeling on Ile, Leu, and Val residues (see Materials and Methods).[23] Complete backbone resonance assign-

ments have been determined for 107 of the 147 residues, while 38 residues have been partially assigned. Most of the partially assigned residues miss only their $^{13}C'$ assignment such that almost complete $^{1}H^{N}$ (97%), ^{15}N (90%), and $^{13}C^{\alpha}$ (95%) assignments have been determined. Importantly, peaks for 135 residues have been identified in the HSQC spectra of the amide or methyl regions, providing easily accessible probes for nearly every residue within the KvAP VSD (Fig. 1).

The largely α-helical nature of this protein was observed both in the characteristic pattern of local nuclear Overhauser effect (NOE) cross-peaks in NOESY spectra and in the backbone dihedral angles derived from chemical shifts.[24] However, the inter-helical packing arrangement was uncertain, as many side-chain contacts, especially those between methyl groups exhibiting highly degenerate chemical shifts, were highly ambiguous. To overcome this ambiguity, we divided the structure calculation into two stages (see Materials and Methods for more details). In the first stage, we refined the individual secondary structural elements using only dihedral restraints and unambiguous local distance restraints (consisting of interatomic $^{1}H^{N}$, $^{1}H^{\alpha}$, and $^{1}H^{\beta}$ distances less than five residues apart). From these calculations, four helical regions corresponding to the transmembrane helices S1–S4 were clearly distinguished. We then added unambiguous long-range distance restraints (primarily aromatic–methyl and methyl–methyl interactions) to obtain an ensemble of loosely folded protein structures. During our second stage, we gradually incorporated additional local and long-range distance restraints based on the previously determined set of structures. In this manner, we could steadily reduce or eliminate NOE ambiguities (Table 1 and Fig. 2). The final set of solution KvAP VSD structures is well defined overall, with an average root-mean-square deviation (r.m.s.d.) from the mean coordinates of 1.22 Å for α-carbons in residues P25-K147 (Fig. 3).

Comparison of VSD structures

The solution structure (closest to the mean coordinates) of the KvAP VSD in D7PC micelles closely resembles the crystal structure of the KvAP VSD solubilized in *n*-octyl-β-D-glucoside and complexed to an antibody fragment (Fig. 4a).[7] The first two transmembrane helices, S1 and S2, comprise the region that is most similar between the two structures, with an r.m.s.d. of 1.41 Å for α-carbons in residues H24-E45 (in S1) and residues Y59-Y78 (in S2). The largest deviation within this region is a tilt in the extracellular end of S2 by ~2 Å. Surprisingly, S1 and S2 superimpose much better onto the Kv1.2–Kv2.1 paddle chimera crystal structure,[10] with an r.m.s.d. of 0.84 Å (residues

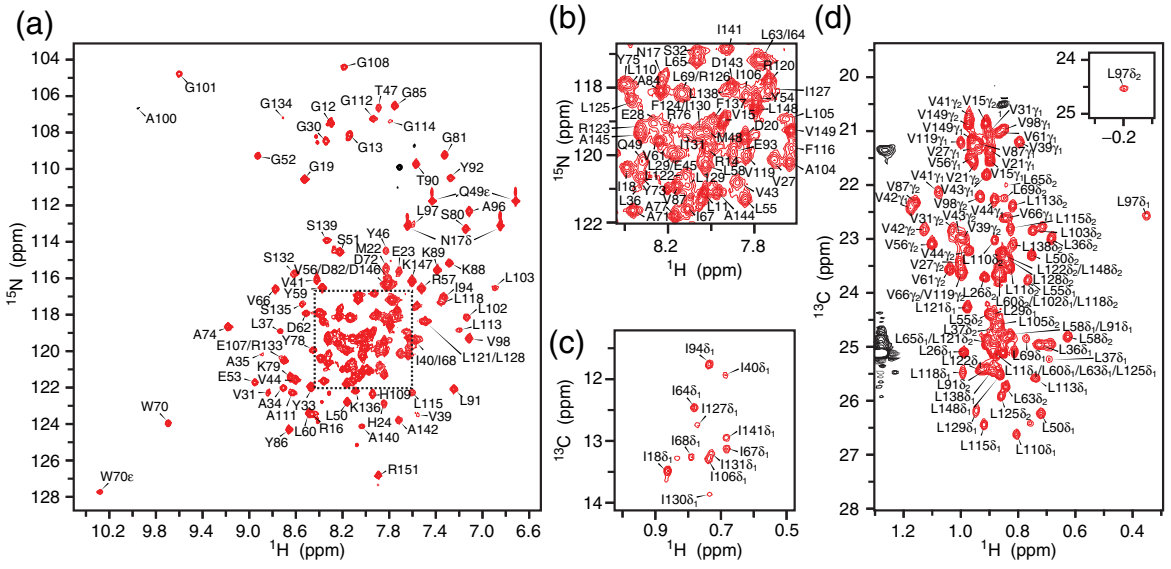

Fig. 1. Amide and methyl resonance assignments for the KvAP VSD in D7PC micelles. (a) ^{1}H–^{15}N HSQC spectrum (21.1 T, 45 °C) of ^{15}N KvAP VSD with assignments. Main-chain amide peaks for 132 residues (out of 141 residues expected to be observed; five Pro) and N17$^{\delta}$, Q49$^{\varepsilon}$, and W70$^{\varepsilon}$ side chains have been assigned. The missing residues are R6-D10, L26, S38, V42, and R117. Peaks that are aliased in the ^{15}N dimension are shown in black (A100 and Arg$^{\varepsilon}$). (b) Enlarged view of the congested area in (a) within the dotted square. (c) ^{1}H–^{13}C HSQC spectrum (21.1 T, 45 °C) of the Ile$^{\delta 1}$ methyl region of $^{2}H,^{13}C^{methyl}$-ILV KvAP VSD in 98% (vol/vol) D_2O with assignments. Methyl peaks for all 11 Ile have been identified. (d) Leu/Val methyl region of the spectrum shown in (c). Peaks for 84 methyl groups (out of 92 peaks expected to be observed from 16 Val and 30 Leu residues) have been identified. Missing assignments include L5$^{\delta 1/\delta 2}$, L8$^{\delta 1/\delta 2}$, L29$^{\delta 1}$, L102$^{\delta 2}$, L103$^{\delta 1}$, L105$^{\delta 1}$, L128$^{\delta 1}$, and L129$^{\delta 2}$. Peaks from D7PC are shown in black.

Table 1. NMR structure and refinement statistics for the KvAP VSD

NMR restraints	
Distance restraints (NOE)	
Intraresidue ($i=j$)	220
Medium range ($\|i-j\| \leq 4$)	777
Long range ($\|i-j\| > 4$)	155
Total	1152
Dihedral restraints (TALOS)	
ϕ	126
φ	126
Total	252
Structure statistics	
Ensemble r.m.s.d. (residues P25-K147)	
Backbone heavy atoms (Å)	1.22
All heavy atoms (Å)	1.61
NOE violations[a]	
≥0.1 Å	42.2 ± 5.5
≥0.3 Å	4.7 ± 2.2
≥0.5 Å	0.0 ± 0.0
r.m.s.d. from experimental restraints[a]	
Distances (Å)	0.041 ± 0.003
Dihedrals (°)	0.3 ± 0.1
r.m.s.d. from idealized geometry[a]	
Bond lengths (Å)	0.004 ± 0.001
Bond angles (°)	0.48 ± 0.02
Impropers (°)	0.34 ± 0.02
Ramachandran plot[b] (residues L11-R151)	
Most favorable (%)	92.0 ± 1.3
Additionally allowed (%)	6.9 ± 1.5
Generously allowed (%)	0.8 ± 0.7
Disallowed (%)	0.1 ± 0.5

[a]Xplor-NIH.
[b]Procheck NMR.

A162-E183 and F223-F242) (Fig. 4b). These helices are especially stable, as amide protons from residues in both S1 (I40, V41, V43, and V44) and S2 (V61-A77) are resistant to exchange with solvent when placed in a D_2O buffer and are likewise absent or have reduced amplitude in the spectra of deuterated samples (Fig. S2).

Before S1, the NMR structure of the KvAP VSD contains a short ~10-residue amphipathic α-helix (S0) that lies approximately perpendicular to the four transmembrane helices. This helix was not modeled in the crystal structure, as no significant electron density was observed for the first 15 amino acids.[7] The helical structure of this region is clearly identified by local NOEs; however, the precise position of this helix is not well determined, as few long-range NOEs were observed. Those that could be identified involve residues at the intracellular end of S2, suggesting that S0 likely resides in a position similar to that of an analogous helix in eukaryotic Kv channels (Fig. 4b).[10] This helix is required for high-level KvAP VSD expression in *E. coli*, as expression is barely detectable with a construct that begins at M22 (removing S0) but is only slightly reduced when only the first 10 residues that precede S0 are removed (data not shown). The amphipathic nature of this helix and its position at the edge of the VSD structure suggest that it interacts with the interfacial region of the D7PC micelle.

The largest difference between the solution structure and the crystal structure occurs in the S3b–S4 "paddle" region. In the structure closest to the mean coordinates, S4 is shifted closer to S2 by ~3 Å, while S3 is farther from S1 by ~5 Å, resulting in a ~23° twist in the orientation of the paddle with respect to S1 and S2 (Fig. 4a). When compared to the NMR ensemble, the crystal structure paddle is an outlier (Fig. S3), and the different paddle positions likely indicate genuine structural variation. The close association between S2 and S4 in solution is evidenced by the many NOEs observed between the side chains of residue Y46 (S2) and the side chains of residues R126 and I127 (S4). For the crystal structure, the KvAP VSD was cocrystallized with an antibody fragment that binds to an epitope at the tip of the paddle.[7,25–27] The altered paddle position reflects the pliability of this region and suggests that the paddle may adopt slightly different conformations, depending on the immediate lipid (or detergent) environment. The overall structure of the paddle remains similar (r.m.s.d. is 0.80 Å for residues A100-R126), suggesting that the paddle is repositioned as a nearly rigid unit. Notably, the positions of R133, K136, and the hydrophobic "phenylalanine gap" residue L69 between them near the center of the domain are in identical locations, suggesting that small changes at the periphery of the protein are not transferred to the central packed core.

Backbone dynamics of the KvAP VSD

Both the crystal structure and the NMR structure of the KvAP VSD reveal a significant kink in the middle of S3 that divides this helix into two separate segments (S3a and S3b). This structural distinction is reflected by paddle antibody inhibition and by avidin accessibility to tethered biotin during KvAP channel activity.[25–27] While residues in S3a remain static throughout the gating cycle, some residues in S3b are externally accessible only when the membrane is depolarized and the channel is open. This region contains a highly conserved Pro residue (P99) and has been suggested to serve as a hinge to permit the movement of S3b and S4 during channel gating.[27,28]

To determine the flexibility inherent in the KvAP VSD, we probed the backbone dynamic properties using TROSY-detected ^{15}N relaxation measurements at 14.1 T. Similar experiments have been performed on the KvAP VSD in DPC/LDAO micelles.[21] Our dynamics data are in excellent agreement with those results. For a large protein–micelle system, the amide longitudinal ^{15}N relaxation rate constants (R_1) and $\{^1H\}$–^{15}N heteronuclear nuclear Overhauser enhancements (hetNOEs) are sensitive indicators of

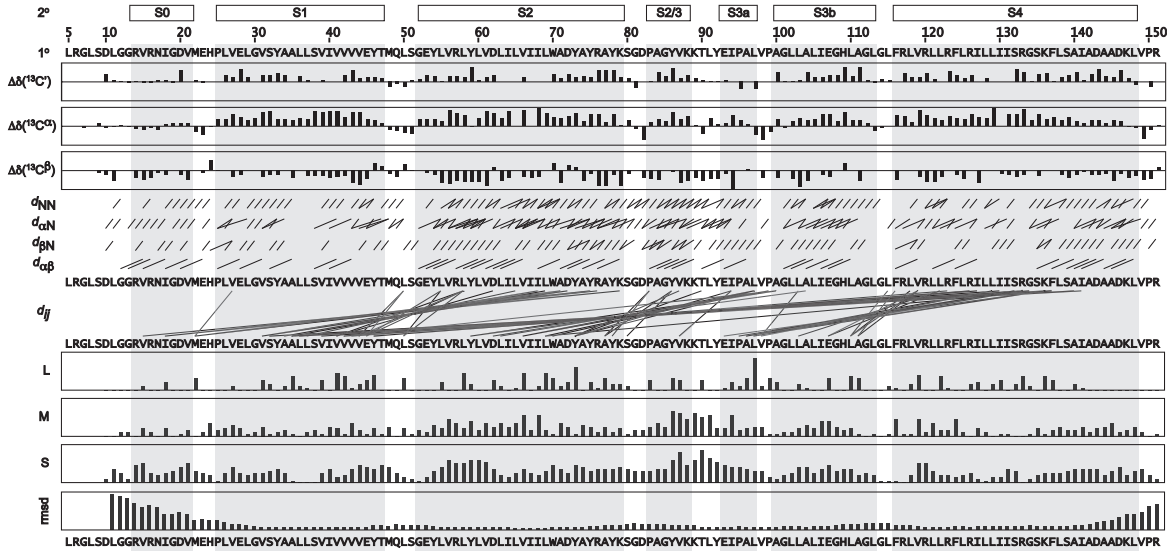

Fig. 2. Summary of NMR restraints used to define the KvAP VSD structure. Secondary structural elements (2°) are shown above the amino acid sequence (1°) and highlighted in gray. The VSD helices are identified by the pattern of secondary chemical shifts for $^{13}C'$, $^{13}C^{\alpha}$, and $^{13}C^{\beta}$ [$\Delta\delta(^{13}C^{X})$; corrected for ^{2}H isotope shifts[59] and graphed from −5 ppm to +5 ppm][60] plotted below the amino acid sequence, and the sequential and medium-range NOE cross-peaks (d_{XY}) are indicated by black lines connecting the residues (subscripts $\alpha = {}^{1}H^{\alpha}$, $\beta = {}^{1}H^{\beta}$, and $N = {}^{1}H^{N}$ indicate the atoms involved; for Pro residues, $^{1}H^{\delta}$ was used in place of $^{1}H^{N}$). The long-range NOE cross-peaks ($d_{i,j}$) defining the tertiary fold are also shown. The total numbers of long-range (L; $|i-j|>4$), medium-range (M; $1<|i-j|\leq 4$), and sequential (S; $|i-j|=1$) NOEs are plotted (graphed from 0 to 20 NOEs) above the ensemble r.m.s.d. from the mean coordinates (for residues L11-R151; graphed from 0 to 10 Å).

fast picosecond-to-nanosecond timescale motion. Residues at the N-terminus and the C-terminus display larger R_1 (>1 s^{-1}) and lower hetNOE (<0.4), characteristic of highly flexible residues (Fig. 5a and b). The S0 helix is also highly mobile, consistent with its poor placement within the NMR ensemble. The S1–S2 loop contains some residues with low hetNOE (<0.6), but the remainder of the protein is relatively rigid, and both the S2–S3 region and the break in S3 have relaxation characteristics similar to those of transmembrane helical elements (the average hetNOE for residues in S1 and S2 is 0.73). Thus, these regions are likely static elements of the structure with little flexibility. The rigidity of the S3 kink suggests that this extended structure is stable on the picosecond-to-nanosecond timescale even in a micelle environment.

One characteristic of amide HSQC (Fig. 1a) is that peaks have a wide range of signal intensities. Several residues within S3, notably L97 within the S3 kink, have significantly lower-than-average signal intensity. Chemical exchange provides an additional relaxation mechanism when a nuclear spin experiences a fluctuating environment and is a sensitive indicator of conformational changes on the microsecond-to-millisecond timescale. To determine if reduced signal intensities are a result of peak broadening due to chemical exchange, we measured amide ^{15}N transverse relaxation rate constants (R_2). Like R_1, R_2 is sensitive to fast timescale motion, as evidenced by the decreased R_2 seen at the N-terminus and the C-terminus (Fig. 5c). However, large outlying R_2 is observed for several residues throughout the VSD, indicating that these sites likely experience additional peak broadening.

We estimated the chemical exchange contribution to R_2 (R_{ex}) using a TROSY-based Hahn-echo transverse relaxation experiment.[29] This method uses the transverse ^{1}H–^{15}N dipolar/^{15}N chemical shift anisotropy interference rate constants (η_{xy}) to determine R_2 rate constants that are independent of chemical exchange (see Materials and Methods and Fig. S4). For most of the residues in the KvAP VSD, R_{ex} rates are close to zero ($|R_{ex}|<5\ s^{-1}$), indicating that chemical exchange is not present (Fig. 5d). Four regions (typified by residues H24, Y75, L97, and L138) have large R_{ex} (>10 s^{-1}) and are mobile on the microsecond-to-millisecond timescale. L97, in particular, has the largest R_{ex}, suggesting that the S3 kink may serve as a hinge in the movement of the paddle in response to changes in membrane voltage.

In the isolated VSD construct, residues R117-K147 form a continuous helix, S4. However, in the full-length channel, S4 is expected to break and form the "S4–S5 linker" helix that connects the VSD to the ion-conducting pore.[8] In the Kv1.2–Kv2.1 paddle chimera crystal structure, this break occurs at residues

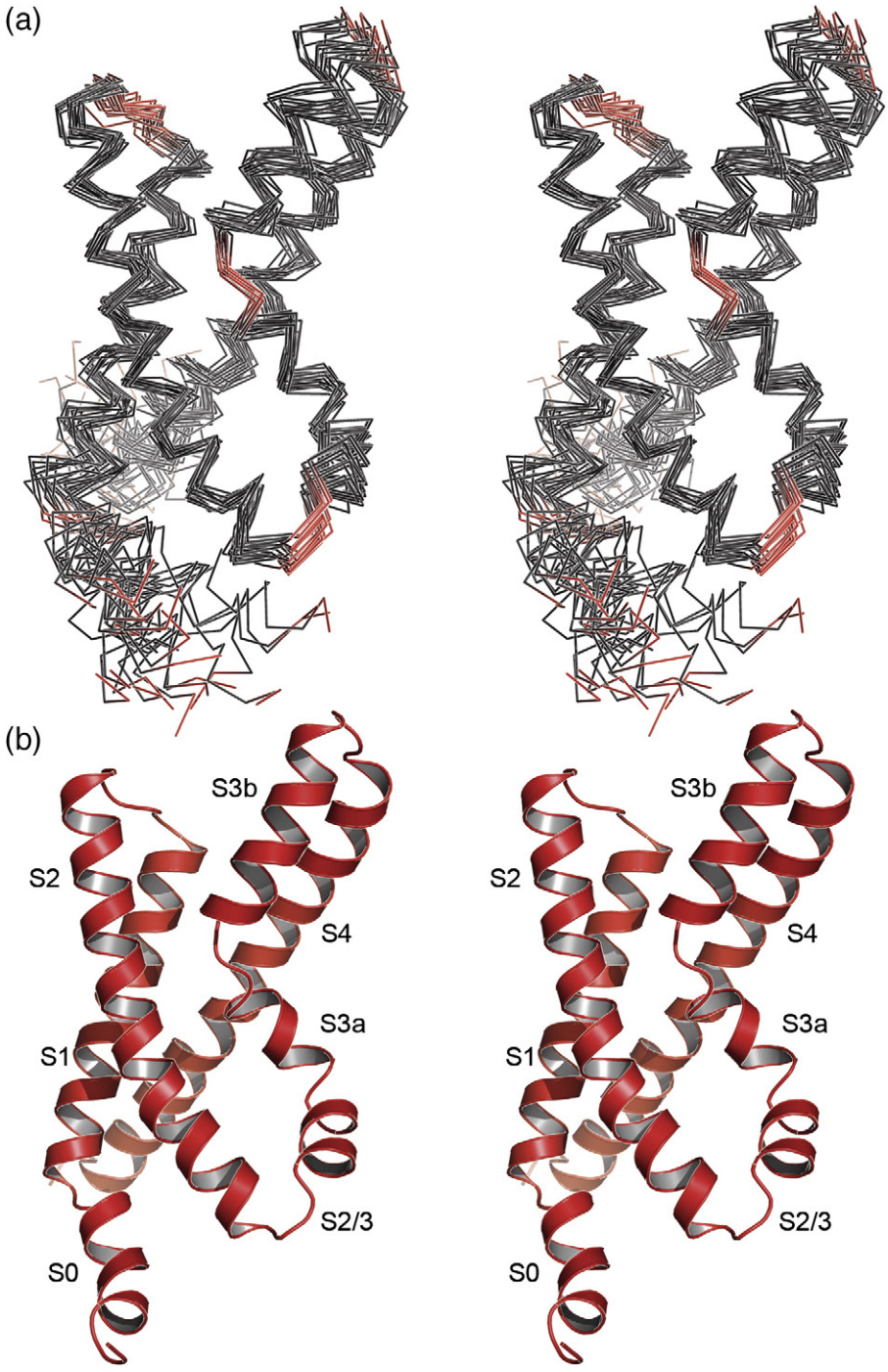

Fig. 3. Solution structure of the KvAP VSD. (a) Stereo image of the 20 lowest-energy structures (α-carbon trace) superimposed using residues P25-K147. Helical segments are shown in dark gray, while loops are shown in red. The first seven residues (L5-D10) are unconstrained (and unstructured in the ensemble) and have been removed for clarity. (b) A ribbon representation of the structure closest to the mean coordinates. The transmembrane (S1, S2, S3a, S3b, and S4) and other helices (S0 and S2/S3) are labeled. This and all other structure figures were generated using the program PyMOL.[61]

H310-K312.[10] In the VSD structural alignment (Fig. 4b), these residues reside near L138, which exhibits chemical exchange peak broadening along with nearby residues. Thus, although the KvAP pore domain has been removed in the VSD construct, it appears that a vestige of the S4–S5 linker remains and that the observed chemical exchange is likely due to transient helix breaks in this region.

Two other regions also exhibit elevated R_2: around residues H24 and Y75. H24 is located in the short

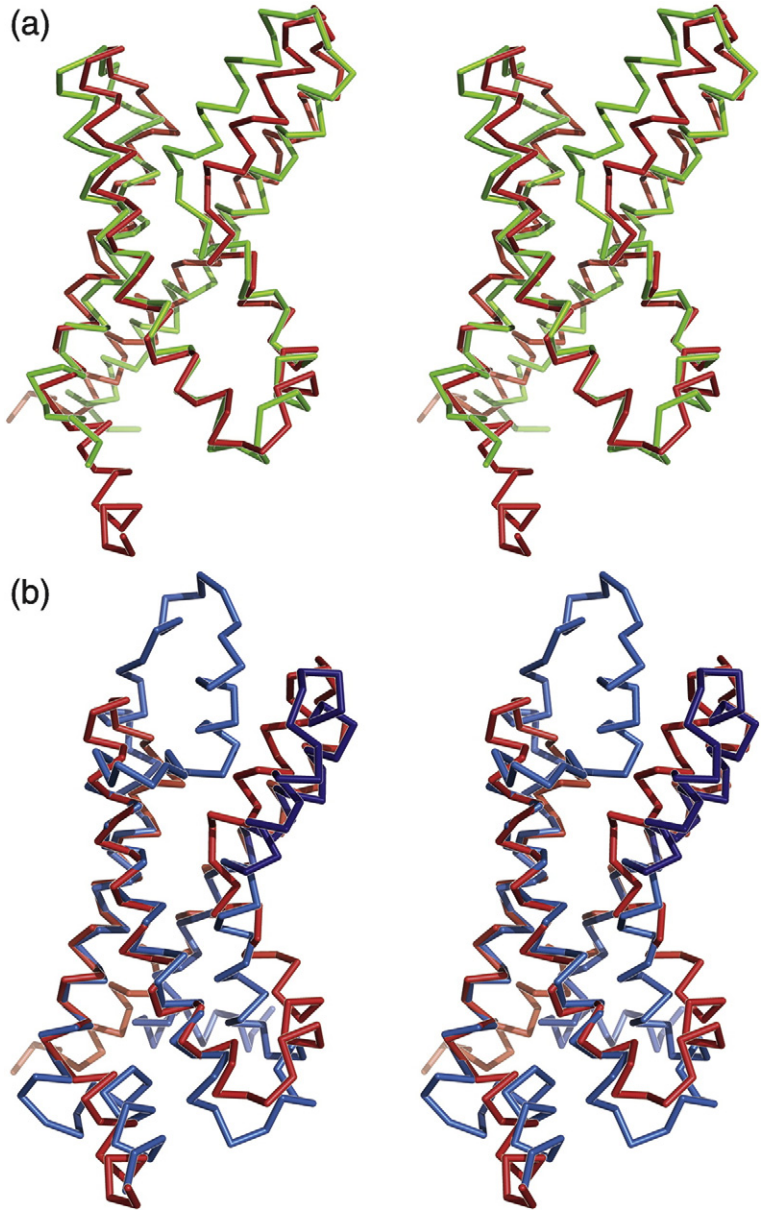

Fig. 4. Comparison of VSD structures. (a) Superpositioning of KvAP VSDs determined by crystallography (chartreuse) and NMR spectroscopy (structure closest to the mean coordinates; red) using α-carbons of residues H24-E45 in S1 and residues Y59-Y78 in S2. (b) Superpositioning of the KvAP VSD NMR structure and the Kv1.2–Kv2.1 paddle chimera VSD crystal structure (using the α-carbons of residues A162-E183 and F223-F242). The Kv1.2 (light blue) and Kv2.1 (dark blue) portions of the chimera are colored separately.

loop between S0 and S1, and Y75 is found at the C-terminal end of S2 and interacts with residues in S0. Thus, these two residues are expected to be sensitive to the position of S0. The chemical exchange peak broadening observed for H24 and Y75 is consistent with the microsecond-to-millisecond timescale repositioning of S0. Combined with high R_1 and low hetNOE, this suggests that S0 exhibits mobility across multiple timescales, further supporting the hypothesis that S0 is dislodged in the absence of a membrane bilayer.

Using the R_2/R_1 ratio for residues in the transmembrane helices, we determined that the KvAP VSD has an isotropic rotational correlation time of 19.8 ± 0.1 ns at 45 °C. This value is close to the 18.4 ns calculated for the KvAP VSD in DPC/LDAO (also at 45 °C),[21] which suggests that the D7PC and DPC/LDAO micelles are of comparable size. Based on similar measurements on soluble globular proteins,[30,31] the KvAP VSD in D7PC micelles has an apparent particle size of approximately 50–60 kDa. This is in agreement with the similarly sized β-barrel proteins OmpX,[32] OmpA,[33] and PagP,[34] and suggests that the KvAP VSD is a monomer under the current conditions.

KvAP VSD–micelle interactions

The NOESY spectra used for calculating the NMR ensemble of structures also contain information regarding water and detergent molecules at the

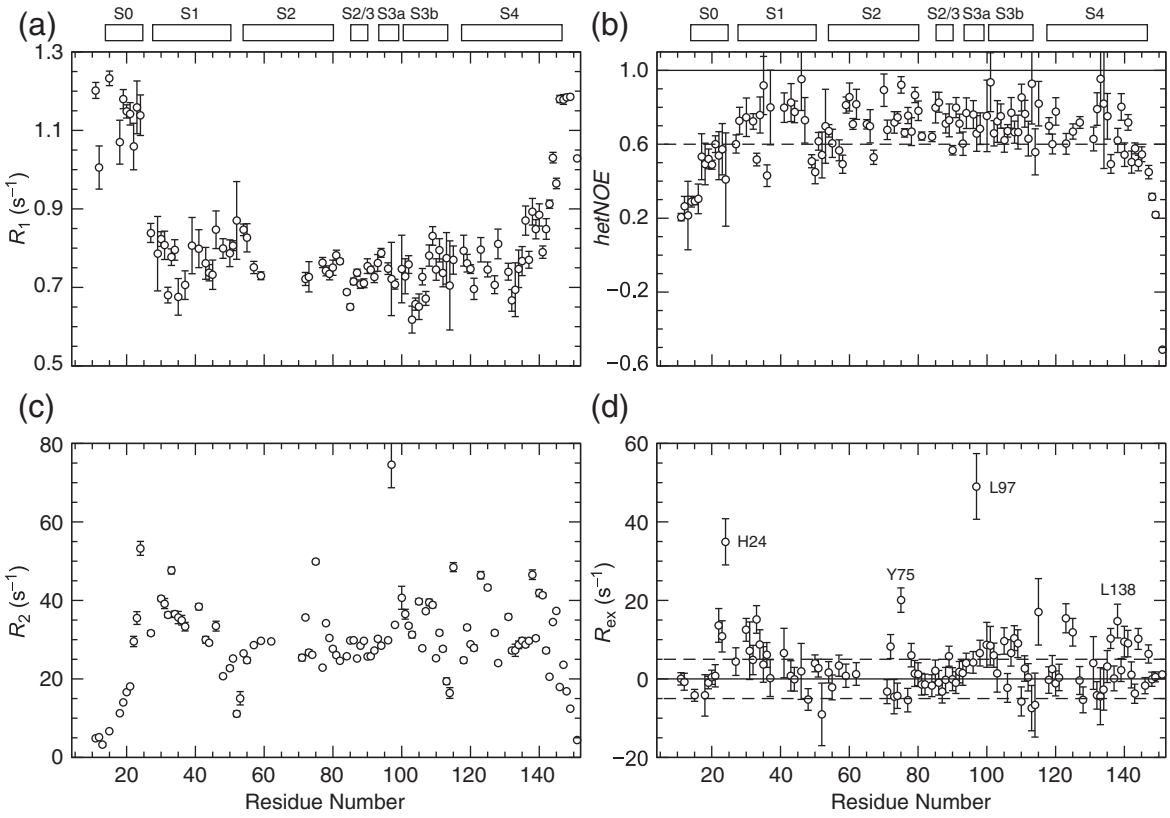

Fig. 5. Backbone dynamic measurements. (a) R_1, (b) hetNOE, and (c) R_2 backbone ^{15}N relaxation measurements for $^{2}H,^{15}N$ KvAP VSD in D7PC micelles (14.1 T, 45 °C) are plotted *versus* residue number. (d) R_{ex} calculated using $\kappa = 1.65 \pm 0.19$ is the average R_2/η_{xy} ratio for residues not subject to chemical exchange line broadening. Select residues with large R_{ex} are labeled. Secondary structural elements are depicted at the top of the figure.

protein surface. In a D7PC micelle, the molecules form a continuous surface that surrounds the KvAP VSD, and individual D7PC molecules cannot be distinguished. While many NOEs at the water resonance could be identified, D7PC resonances (Fig. S8) are overlapped with protein resonances, so an unambiguous assignment of detergent NOEs was impossible for many residues. To overcome this limitation, we utilized a ^{13}C-filtered NOESY experiment[35] whereby protons that are bound to ^{13}C atoms are removed from our spectra. Thus, by using a $^{13}C,^{15}N$ KvAP VSD sample, we eliminated most protein NOEs, leaving only detergent NOEs in the aliphatic portion of the spectrum. Notably, we did not filter out signals from protons attached to ^{15}N nuclei so that NOEs to amide $^{1}H^{N}$ could be used to confirm our assignment of the protein resonance.

Inspection of water and detergent NOEs reveals a noticeably graded pattern (Fig. 6). Consistent with the native transmembrane locale of the VSD, NOEs to water and the hydrophilic choline headgroup and glycerol backbone portions of D7PC are restricted to the intracellular and extracellular ends of the VSD (Fig. 6a–c). NOEs at the water resonance may be the result of a direct interaction with water (either via NOE or via physical exchange of a proton) or an NOE to a nearby group that exchanges with water (a relayed NOE). In either case, water NOEs indicate regions of the protein that are near an aqueous environment. NOEs to the aliphatic tails of D7PC are distributed throughout much of the protein and are particularly dense along the transmembrane helices (Fig. 6d and e). Many residues have NOEs to multiple D7PC protons due to the dynamic nature of the micelle structure and ^{1}H spin diffusion within individual D7PC molecules. Nevertheless, there is a subtle distinction between NOEs to the two aliphatic positions closest to the glycerol backbone (Fig. 6d) and NOEs to the last four positions that include the methyl tail (Fig. 6e). Although many residues exhibit NOEs to both sets of aliphatic protons, residues near the ends of the helices typically have more intense NOEs to the first two positions, while the reverse is true for more centrally located residues.

With the use of only the transmembrane helices (S1–S4), the distribution of NOEs along the transmembrane axis of the KvAP VSD closely resembles the dimensions of a lipid bilayer (Fig. 6f). NOEs to the aliphatic tails of D7PC are observed over a span of 30 Å, centered about the middle of the VSD

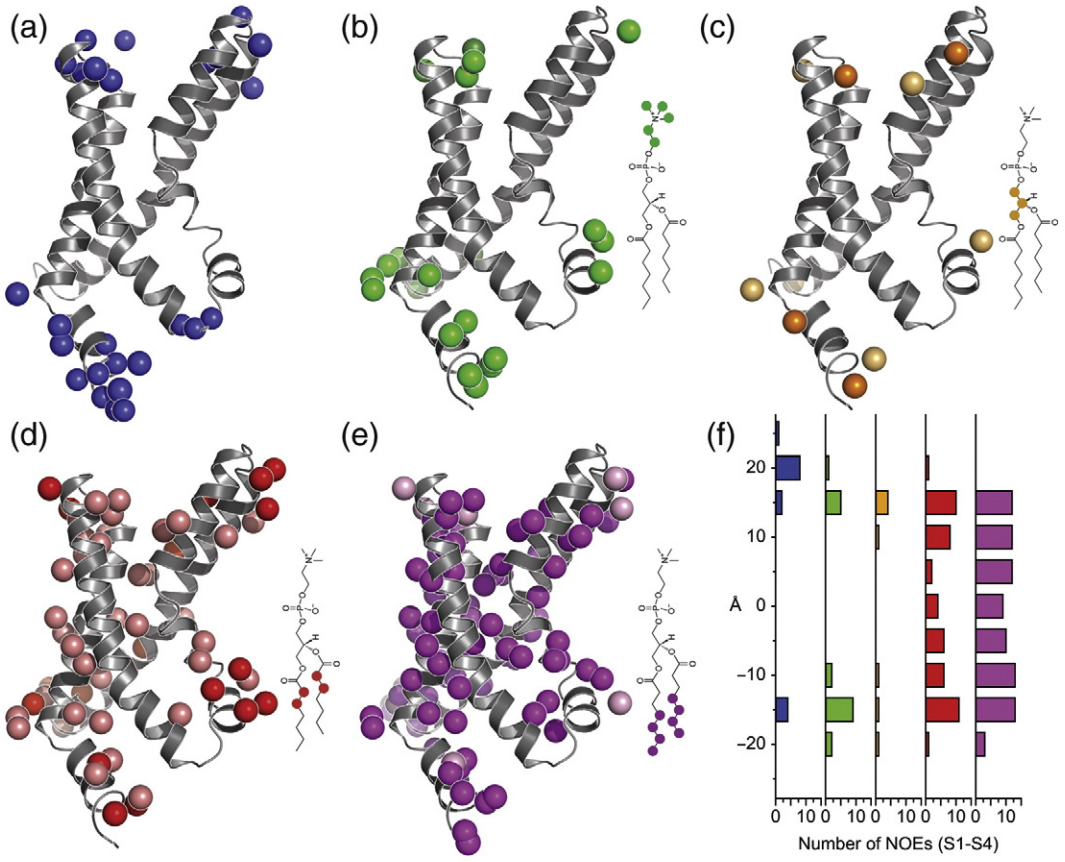

Fig. 6. VSD–micelle interactions. NOE cross-peaks to (a) water and to the (b) choline headgroup, (c) glycerol backbone, (d) the first two aliphatic carbons, and (e) the last four aliphatic carbons of D7PC are mapped onto the solution structure of the KvAP VSD. The diagram highlights the regions of D7PC included in mapping (not drawn to scale). For NOEs to D7PC, the peak intensities were normalized by the number of D7PC protons, and the single most intense NOE is shown in a darker color. (f) Histogram of NOEs to the transmembrane helices (S1–S4) as a function of distance from the center of the VSD.

(approximated by residues V39, I64, V98, and I131 in S1–S4, respectively). NOEs to the hydrophilic headgroup and backbone occur within a 10-Å segment on both sides of the VSD, overlapping with aliphatic NOEs by 5 Å and providing a total thickness of 40 Å. Consequently, the D7PC micelle approximates the dimensions and chemical environment of a membrane bilayer.[36]

Paramagnetic phospholipid interactions

To investigate KvAP VSD interactions with bilayer-forming lipids, we initially added several different lipids into D7PC-solubilized ^{15}N KvAP VSD in a stepwise fashion. While we observed changes in many peak positions in HSQC spectra, incorporation of more than a few millimolars of lipids significantly reduced signal intensities and degraded the overall spectral quality. As an alternative approach to studying long-chain lipid interactions, we chose to incorporate paramagnetically labeled lipids into KvAP VSD samples.[37] Freely diffusing lipids have the opportunity to interact with the entire hydrophobic surface of the protein, and the paramagnetic enhancement in spin relaxation (ε) is a combined function of both average distance and residence time. A similar method, using paramagnetically labeled fatty acids, has been used successfully to study the lipid-interacting surface of OmpX[38] and membrane-associated peptides.[39,40]

The stepwise addition of 1-palmitoyl-2-stearoyl-*sn*-glycero-3-phosphocholine (PSPC) to the paramagnetic group doxyl incorporated into position 16 of the stearoyl chain (16-doxyl PSPC) elicits a significant decay in signal intensities for many residues in the KvAP VSD (Fig. 7a). To determine the relaxation enhancement, we used the peak intensity ratio from separate 16-doxyl PSPC (I_{doxyl}) and PSPC (I_{PSPC}) titrations. PSPC titration was used to control for small but measurable shifts in peak positions and to account for any changes in the

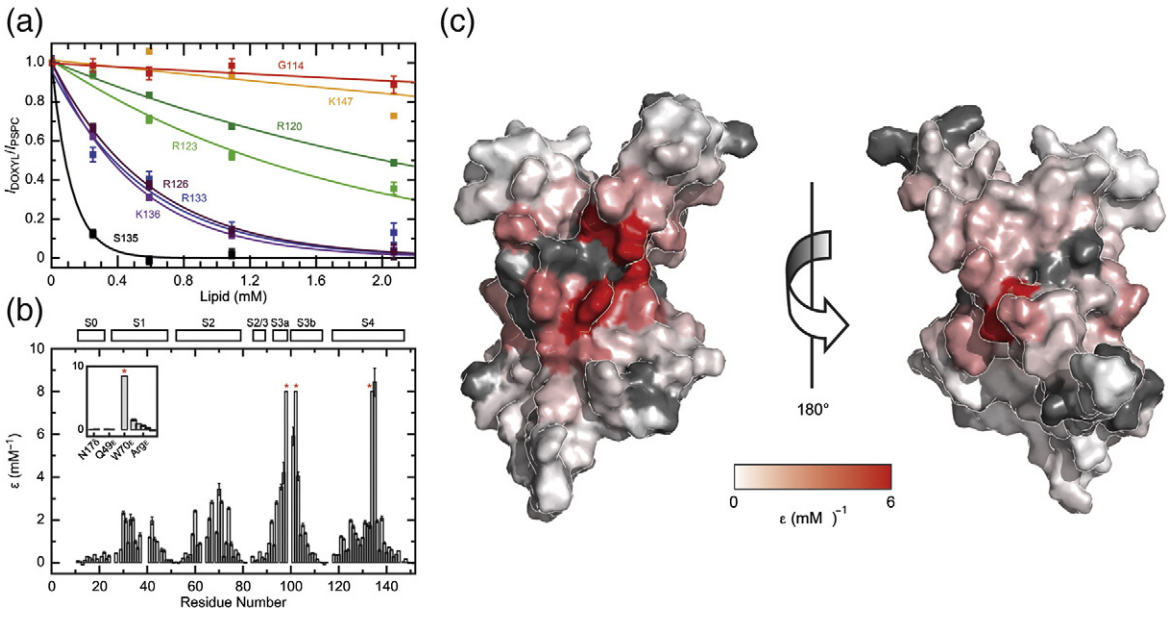

Fig. 7. Paramagnetic lipid titration. (a) Measurement of paramagnetic relaxation enhancement ε for residues along S4 in the [^{15}N]GSRKF KvAP VSD sample. (b) Relaxation enhancement values are plotted for all residues. Inset: ε for selected side chains. For some peaks (indicated by a red asterisk), ε was too large to be measured, and the bar is drawn to 8 mM^{-1}. Secondary structural elements are depicted above the graph. (c) Data in (b) mapped onto the surface of the KvAP VSD using a linear gradient between white (ε = 0 mM^{-1}) and red (ε ≥ 4 mM^{-1}). Residues with unknown ε are shown in gray. The left image is in the same orientation as Fig. 3b.

sample over time. We limited the amount of lipids to only a few lipid molecules per micelle so that the relaxation enhancement is proportional to the bulk concentration of lipids. Although the lipids are not likely bilayered in nature at these concentrations, the magnitude of ε provides a measure of the relative affinity for long-chain lipids at a given region of the protein.

Due to the large degree of overlap in ^{1}H–^{15}N HSQC spectra, we employed several samples with different combinations of labeled amino acids to adequately probe the VSD. Aside from a uniformly labeled ^{15}N sample, we used ^{15}N-labeled Gly, Ser, Arg, Lys, and Phe ([^{15}N]GSRKF) samples, and ^{15}N-labeled Gly, Ser, Ala, Ile, Leu, and Val ([^{15}N]GSAILV) samples. These were purified exactly in the same way and contained sets of overlapping residues that exhibited matching relaxation enhancement (Fig. S6), thus establishing the reproducibility of our measurements.

Titration data for residues in S4 illustrate the typical behavior of the transmembrane helices (Fig. 7a): ε is close to zero near each end of the helix and gradually increases for residues deeper in the micelle. This basic mounded feature clearly distinguishes all four transmembrane helices, and the apices identify the center of each helix (Fig. 7b). In S4, G134 and S135 have the maximum relaxation enhancement where the signal is almost completely eliminated at our first data point (estimated to be ~1 lipid per micelle). When mapped onto the KvAP VSD solution structure (Fig. 7c), the helical centers cluster to the middle of the domain and likely represent the most centrally located portion of the VSD when embedded in a membrane bilayer.

One prominent feature of paramagnetic relaxation properties is that the maximal ε is not the same for each of the four transmembrane helices. For S1 and S2, the maximum ε is ~3 mM^{-1}, whereas residues in both S3 and S4 have an ε that is larger than what we could measure (~8 mM^{-1}). This suggests that helices S3 and S4 interact more favorably with the spin-labeled PSPC than do S1 and S2. This discrepancy between helical segments is not due to the doxyl group alone, as a similar titration using a doxyl-labeled fatty acid did not show such a pronounced difference in relaxation enhancements (Fig. S7).

Discussion

The goal of this study was to provide a comprehensive description of a VSD within the context of a phospholipid environment. Although a high-resolution crystal structure of the KvAP VSD had already been determined,[7] it was unclear whether this structure represents the native membrane-embedded conformation, since it was solubilized in a nonionic detergent and complexed with an

antibody. Antibodies to the paddle inhibit KvAP activity by locking the VSD in a conformation that presumably resembles an inactivated state of the channel.[11,26] It has been shown that KvAP cannot function in the absence of phospholipids, and the addition of intermediate-chain 1,2-didecanoyl-*sn*-glycerol-3-phosphocholine is sufficient to restore channel function.[14] In our present case, the phospholipid environment is micellar in nature, so the physical properties of a membrane bilayer are not entirely native, but the chemical features surrounding the KvAP VSD should be similar to those of a membrane. This proved to be a fruitful approach as the solution and crystal structures exhibit several differences throughout the VSD. By comparing these two structures, we can provide insight into the natural conformational variability found within this domain.

An emerging theme in Kv channel structure is the conformational freedom of the S3b–S4 paddle.[41] This region occupies a diverse set of conformations relative to the rest of the domain in crystal structures of Kv VSDs[7,8,10] and other related channels.[42] This region is unique because it exists outside the set of coevolved residues in the Kv family,[28] and this segment can be transferred among Kv (and related) channels while maintaining function.[43] The slightly different conformations observed under solution and crystal experimental conditions provide further support for its inherent mobility. The different paddle positions observed in other Kv and related channels are not solely due to differences in the amino acid composition of this region but also appear due to its flexibility as a unit.

One significant similarity between the solution structure and the crystal structure is the presence of the kink in S3. This elongated structure persists over four residues (L97-A100) that reside in the middle of the micelle. Residues at each end of this extended sequence (V98 and L102) are some of the most strongly affected by the spin-labeled lipids and are expected to reside at the center of the membrane. The fact that this extended conformation exists in both structures and is relatively ordered on the picosecond-to-nanosecond timescale signifies its stability in a micelle environment. The irregularity of this structure and the presence of a highly conserved Pro residue have led to the suggestion that this region acts as a hinge in the movement of the paddle. The chemical exchange peak broadening observed for L97 (Fig. 4b), which is consistent with motion on the microsecond-to-millisecond timescale, provides experimental support for this hypothesis.

The solution structure identified an additional α-helix in the KvAP VSD at the N-terminus (S0) that is also observed in the Kv1.2–Kv2.1 paddle chimera structure.[10] This helix was not modeled in the KvAP VSD crystal structure, perhaps because its flexibility across multiple timescales prevented significant electron density to be observed. S0 is roughly positioned between the intracellular end of S1 and the intracellular end of S2, and the mix of NOEs with water, hydrophilic D7PC resonances, and hydrophobic D7PC resonances establishes its interfacial location. This helix is conserved among other VSDs, and, in the context of a membrane bilayer, this helix may perform a structural role in supporting S1 and S2. This helix-forming segment is required for high-level KvAP VSD expression, and we suggest that it is an integral part of the VSD overall fold.

Using the solution structure as our reference, we characterized the protein–phospholipid micelle interactions in atomic detail. We observed an expected pattern of NOE cross-peaks: water and hydrophilic D7PC NOEs were observed only for the most intracellular and extracellular portions of the VSD, and the transmembrane segments were encircled by NOEs to the aliphatic D7PC chains. The hydrophobic boundary identified by these experiments is ~33 Å, which is similar to the hydrophobic thickness of a membrane but is much longer than the hydrophobic tails of D7PC (~7 Å). A similar incongruity was observed for OmpX within 1,2-dihexanoyl-*sn*-glycerol-3-phosphocholine micelles[32] and suggests that the hydrophobic surface of the protein determines micelle size. This analysis provides a clear description of the micellar environment surrounding the VSD and suggests that the solution structure of the VSD approximates a membrane-embedded conformation under these conditions. This conclusion is further supported by the similarity in amide peak positions in HSQC spectra between this sample and the KvAP VSD embedded in lipid–protein nanoparticles.[44]

Using paramagnetically labeled phospholipids, we identified the primary interaction sites for bilayer-forming lipids. In a native membrane, closely associated lipids engulf the entire outer perimeter of the VSD. Indeed, electron paramagnetic resonance accessibility studies suggest that all four transmembrane helices are equally exposed to the lipid environment in the isolated KvAP VSD.[19] However, the experiments shown here suggest that these lipids will not interact uniformly along the transmembrane surface of the KvAP VSD.

The larger apparent affinity for PSPC along S3 and S4 might reflect a greater actual affinity for phospholipids near this region. Although it is unknown which segment of PSPC would be specifically recognized by the VSD, the phosphatidylcholine headgroup and glycerol backbone are likely candidates due to the abundance of possible specific interactions. As KvAP channel activity is abolished in the absence of a phospholipid membrane, Arg–phosphate interactions along S4 could provide a mechanism for increased phospholipid affinity in this region. In this case, D7PC molecules

might also bind to this site but remain undetected in the absence of a doxyl group. The association of lipid molecules is expected to be intermediate to fast on the chemical shift timescale, since separate lipid chemical shifts are not observed in the NOESY spectra for residues S3 and S4. This timescale is consistent with the small but significant R_{ex} values observed for many residues in S3b and S4 (Fig. 5d).

Alternatively, instead of a specific lipid binding site, PSPC might compete less effectively with D7PC along S1 and S2 than along S3 and S4. The surface hydrophobicities of the four transmembrane helices in the KvAP VSD are similar, with the regions most strongly affected by doxyl PSPC being slightly hydrophilic (Fig. S9). The S1 and S2 helices might present a generic hydrophobic surface that is more equally satisfied by detergents and long-chain lipids. These are stable helices that are immobile during the gating cycle of Kv channels and may buttress the VSD during the movement of the paddle and other regions of the protein.[27,28] This may be a general feature of similar supporting helices in that their conformation and dynamic properties are less connected to the membrane milieu. In contrast, S3 and S4 could have less uniform hydrophobic surfaces that might partially be a result of an irregular structure within the membrane. Although S4 is fully α-helical in the KvAP VSD structures determined to date, a 10-residue segment of S4 exists as a 3_{10}-helix in the Kv1.2–Kv2.1 paddle chimera crystal structure, and an α-to-3_{10} transition has been proposed to move the gating charges across the lipid bilayer.[10]

While we do not know the precise mechanism by which PSPC asymmetrically interacts along the transmembrane surface, it appears that S3 and S4 have a more specific interaction with phospholipids. Thus, these helices are more sensitive to the immediate lipid environment and may be responsible for the altered channel behavior in the presence of different lipids and different mechanical states of the membrane. Further experiments are needed to delineate the specific mechanisms by which the KvAP VSD interacts with the lipid environment.

NMR spectroscopy has become a valuable technique for the study of integral membrane proteins. Here we used NMR to determine the structure and dynamics of a VSD and to characterize its interactions with short-chain and long-chain phospholipids in the context of a phospholipid micelle. The atomic description of the micelle environment and the difference in affinity for membrane lipids along the protein surface likely could not have been obtained using other methods. The approach used here is broadly applicable and is expected to provide additional insight into the structure, dynamics, and lipid interactions of other integral membrane proteins.

Materials and Methods

KvAP VSD sample preparation

To produce uniform isotopically enriched KvAP VSD samples, we grew XL-1 Blue cells (Stratagene), which were transformed with an expression vector,[7] in LB broth at 37 °C until the optical density (measured at 600 nm) had reached ~0.8. The cells were then centrifuged for 10 min at 3000*g* and resuspended in a half volume of M9 minimal medium (concentrating the cells twofold) supplemented with 1 g L^{-1} ISOGRO (Sigma-Aldrich) and 10 mg L^{-1} thiamine using the appropriate isotopic enrichment, as needed. After 1 h, protein expression was induced by the addition of 0.5 mM isopropyl-β-D-thiogalactopyranoside, and the cells were harvested 12–16 h later. By comparing the spectra of deuterated and nondeuterated samples, we estimated the average deuterium incorporation to be ~50% at nonexchangeable sites but greater than 90% at the α positions.

For amino-acid-specific and methyl-specific labeling patterns, a similar expression procedure was employed. For specific labeling of amino acids, the ISOGRO supplement was omitted, the isotopically enriched amino acid (sodium salt) was included in the M9 media at 50–100 mg L^{-1}, and all nonlabeled amino acids were included at 100–200 mg L^{-1}. Similarly, to specifically label the $Ile^{\delta 1}$ and/or $Leu^{\delta}/Val^{\gamma}$ groups (denoted $^{13}C^{methyl}$), we added 50 mg L^{-1} sodium 2-keto-4-^{13}C-butyrate (for Ile) and 100 mg L^{-1} sodium 2-keto-3-methyl-d_3-4-^{13}C butyrate (for Leu/Val) in lieu of their respective amino acids.[23] It should be noted that for Leu^{δ} and Val^{γ} methyl groups labeled in this manner, one group within the pair is $^{13}CH_3$, while the other is $^{12}CD_3$.

For all samples, the KvAP VSD was purified essentially as described previously,[7] with the desired detergent and buffer components adjusted during the final Superdex 200 gel-filtration purification step. Initial screening of detergent conditions used 20 mM Tris (pH 8.0), 100 mM KCl, and detergent concentrations at least twice the critical micelle concentration. The optimized conditions consisted of 20 mM 4-(2-hydroxyethyl)-1-piperazine ethanesulfonic acid (Hepes) (pH 7.0), 20 mM KCl, and 5 mM D7PC. Fractions containing the KvAP VSD were concentrated to between 0.1 and 0.5 mM, and 10 mM 4,4-dimethyl-4-silapentane-1-sulfonic acid was added as internal reference. For samples purified in H_2O, 10% (vol/vol) D_2O was also added. For all samples, the detergent concentration listed is that of the gel-filtration buffer. The final KvAP VSD samples consist of 147 residues: L5-K147 from KvAP plus a remnant of the thrombin site (LVPR) attached to the C-terminus. We note that a Leu (L5) replaces the first five residues in the KvAP coding sequence MARFR.[7]

NMR data collection and analysis

NMR experiments were performed at the New York Structural Biology Center using Bruker Avance or Avance II instruments operating at static magnetic field strengths of 14.1, 18.8, and 21.1 T, equipped with *z*-shielded gradient triple-resonance TCI or TXI cryogenic probes. The sample temperature was maintained at 25 °C during the initial screening of detergent and buffer conditions, and at 45 °C

for all other experiments. NMR spectra were processed using the NMRPipe software package[45] and analyzed using the program SPARKY.[46]

Chemical shift assignments

Resonance assignments for backbone $^{1}H^{N}$, ^{15}N, $^{13}C'$, and $^{13}C^{\alpha}$, and $^{13}C^{\beta}$ nuclei were identified using three-dimensional (3D) TROSY HNCA (at 21.1 T), HNCO, HN(CO)CA, and HNCACB (at 18.8 T) experiments[22,47] performed on 0.3 mM $^{2}H,^{13}C,^{15}N$ samples. Also, two-dimensional (2D) TROSY HSQC and 3D ^{15}N-edited NOESY (mixing times $\tau_{mix}=80$ and 200 ms) experiments (at 21.1 T) were recorded on a 0.3 mM $^{2}H,^{15}N$ sample. In addition to uniformly labeled samples, 2D HSQC, HNCA, and HNCO experiments (at 18.8 T) were recorded on 0.3 mM samples with varied amino-acid-specific labeling patterns designed to eliminate ambiguities: (1) $^{13}C,^{15}N$ Arg; (2) ^{15}N Ile, 1-^{13}C Val, 2-^{13}C Leu; and (3) 1-$^{13}C,^{15}N$ Leu, 2-^{13}C Gly, 2,3-^{13}C Ala. For the 3D experiments, 1024×25 to 1024×32 complex points were collected in the observed $^{1}H\times^{15}N$ dimensions with spectral widths of 12.5 ppm × 25.6 ppm. In the ^{13}C dimensions, 64, 64, 50, and 48 complex points with spectral widths of 15, 23, 16, and 10 ppm were used for HNCA, HNCACB, HN(CO)CA, and HNCO, respectively. The NOESY experiments also used 128 complex points and a spectral width of 12.5 ppm in the indirect ^{1}H dimensions. The 2D experiments using specific amino acid labels were performed with approximately twofold more complex points in the indirectly detected dimensions.

Side-chain resonance assignments were based on 3D HC(C)H-COSY ^{13}C-edited (aromatic and aliphatic) and ^{15}N-edited ($\tau_{mix}=80$ ms) NOESY experiments (at 21.1 T) recorded on 0.5 mM $^{13}C,^{15}N$ samples in 99.9% (vol/vol) D_2O and on a 3D ^{15}N-edited ^{1}H–^{1}H NOESY ($\tau_{mix}=80$ ms) experiment (at 21.1 T) recorded using a 0.5 mM ^{15}N sample. To improve resolution within the Val and Leu methyl regions, we recorded a 3D ^{13}C-edited NOESY ($\tau_{mix}=100$ ms) experiment on a $^{13}C^{methyl}$-LV sample. HC(C)H-COSY was performed with $512\times96\times64$ complex points and 7.8 ppm × 7.8 ppm × 44 ppm spectral widths in the observed $^{1}H\times$ indirect $^{1}H\times^{13}C$ dimensions. The NOESY experiments used 1024×256 complex points and 12.5 ppm × 10 ppm to 12.5 ppm × 12.5 ppm spectral widths in the observed × indirect ^{1}H dimensions, and 32, 64, 48, and 32 complex points for the ^{13}C (aromatic), ^{13}C (aliphatic), ^{15}N, and ^{13}C methyl dimensions with spectral widths of 22, 30, 25.6, and 15 ppm, respectively. Stereochemical assignments for Leu and Val methyl groups were determined using 2D ^{1}H–^{13}C constant-time HSQC experiments (at 21.1 T), with constant-time periods set to 13.3 ms ($\approx 1/^{1}J_{CC}$) and 26.6 ms ($\approx 2/^{1}J_{CC}$), recorded on a 10% ^{13}C fractionally labeled sample in 99% (vol/vol) D_2O.[48] The same HC(C)H-COSY and ^{13}C-edited NOESY experiments were also used to assign the D7PC resonances (see Fig. S8).

Structure calculations

Structure calculations were carried out using the simulated annealing protocol in Xplor-NIH[49,50] and chemical shift-derived dihedral and NOE-derived distance restraints. Backbone ϕ and φ dihedral restraints were determined from ^{15}N, $^{13}C'$, $^{13}C^{\alpha}$, and $^{13}C^{\beta}$ chemical shifts using the program TALOS.[24] Unambiguous ("good") matches were used, and the error for the dihedral restraint was adjusted to at least 20°. Internuclear ^{1}H–^{1}H distance restraints were determined from the signal intensities in NOESY spectra. A wide range of peak amplitudes, where residues that reside within the hydrophobic interior of the micelle generally exhibit a significantly reduced signal intensity, was observed. To reduce underestimation of interproton distances, we first divided the NOE peaks into two groups of residues based on their signal intensities in 2D spectra: one group consisted of residues from the four transmembrane helices and short intervening loops, and the other contained residues from the N-terminus and the C-terminus, S0, and residues between S2 and S3b. Within each set of residues, signal intensities were corrected for the number of protons contributing to the peak and, based on peaks arising from known distances, categorized as strong, medium, weak, and very weak, corresponding to distance ranges of 1.8–2.8, 1.8–3.5, 1.8–4.5, and 1.8–5.5 Å, respectively. Distance restraints were represented by a $(\sum r^{-6})^{-1/6}$ sum over all contributing protons.

The structure calculation process was divided into two stages. Initially, beginning from an extended structure, we defined the secondary structural elements using only backbone dihedral angles and unambiguous local distance restraints (among $^{1}H^{N}$, $^{1}H^{\alpha}$, and $^{1}H^{\beta}$ atoms less than five residues apart). A loosely folded set of structures was obtained by addition of unambiguous long-range distance restraints. In these calculations, the temperature was set to 3500 K for 20 ps (time step , 10 fs) with the following force constants k: $k_{bond\ angle}=0.4$ kcal mol^{-1} deg^{-1}; $k_{improper}=0.4$ kcal mol^{-1} deg^{-2}; $k_{backbone\ dihedrals}=5$ kcal mol^{-1} rad^{-1}; $k_{NOE}=20$ kcal mol^{-1} Å^{-1}. The physical energy term constants were ramped during an additional 2 ps: $k_{atom\ radii}=0.4$-fold to 0.8-fold; $k_{van\ der\ Waals}=0.004$–4 kcal mol^{-1} Å^{-2}; $k_{bond\ angle}=0.4$–1.0 kcal mol^{-1} deg^{-1}; $k_{impropers}=0.4$–1.0 kcal mol^{-1} deg^{-2}. In the subsequent cooling steps, the temperature was lowered to 100 K in 25-K decrements, while the NOE potential constant was ramped from 20 to 30 kcal mol^{-1} Å^{-2}, and the dihedral angle force constant was set to 200 kcal mol^{-1} rad^{-1}. Each round of calculations produced 100 structures, and the 20 lowest-energy structures were chosen to represent the ensemble.

The tertiary fold was gradually refined using successive rounds of calculations with additional local and long-range distance restraints. Each round of calculations was performed starting from the lowest-energy structure determined in the first stage. Additional "unambiguous" restraints were added only if a single assignment was present within 7 Å in the structure ensemble. We also incorporated ambiguous restraints with up to three possible assignments. After each round of calculations, the NOE assignments were reevaluated and adjusted as necessary. These calculations were performed in a similar manner as described above, with the following modifications. The initial high temperature was 3000 K for 10 ps (time step, 2 fs) and cooled to 25 K in 12.5 -K decrements. The van der Waals terms were used throughout the calculation, with radii force constants beginning at 0.9-fold and ramping to 0.8-fold during the cooling steps. Additional torsion angles[51] (ramped 0.002–1) and hydrogen-bonding potentials[52] were also added. Although the second round of calculations was performed starting from a partially folded structure, an

equivalent set of structures is obtained using the final set of restraints starting from an extended structure (the r.m.s.d. for α-carbons in P25-K147 is 1.2 Å between the two lowest-energy structures).

Relaxation rate and diffusion measurements

Amide relaxation measurements used 0.3 mM $^{2}H,^{15}N$ KvAP VSD samples (at 14.1 T). R_1 and R_2 relaxation rates and hetNOE were measured using standard sequences modified for TROSY-based detection of the signal[22] with 512 × 150 complex points and 12.5 ppm × 25.6 ppm spectral widths in the $^{1}H \times ^{15}N$ dimensions. Nine R_1 experiments incorporated relaxation delays between 0.02 and 1.5 s, while 10 R_2 experiments used delays between 8 and 92 ms at an interval of $\tau_{cp} = 1$ ms between the centers of nitrogen pulses in the Carr–Purcell–Meiboom–Gill pulse train. R_1 and R_2 rate constants were determined by the best single-exponential fit to the signal intensities using the program Curvefit.[53] Uncertainties in the rate constants were estimated using a Monte Carlo algorithm, with the error in signal intensity approximated by baseline noise. The proton-saturated and unsaturated hetNOE experiments were collected in an interleaved manner. Four experiments, with the average and standard error taken as hetNOE and uncertainty, respectively, were performed.

The η_{xy} rate constants were measured using a TROSY-based Hahn-echo sequence[29] with 512 × 150 complex points and 12.5 ppm × 25.6 ppm spectral widths for the $^{1}H \times ^{15}N$ dimensions and a relaxation delay of 21.6 ms. Four experiments, with the average and standard error taken as rate constant and uncertainty, respectively, were performed. The chemical exchange contribution was determined as $R_{ex} = R_2 - \kappa\eta_{xy}$, where $\kappa = 1.65 \pm 0.19$ is the average R_2/η_{xy} ratio for residues not subject to chemical exchange line broadening (generally residues with $R_2 < 35\ s^{-1}$; see Fig. S4).

R_2/R_1 ratios for residues within helical segments were used to calculate rotational diffusion time using the local diffusion approach[54] implemented in the program r2r1_diffusion.[53] An isotropic diffusion model was assumed, as little improvement was observed using an axially symmetric model.

D7PC NOE measurement

The 3D ^{13}C-filtered NOESY experiment (at 18.8 T) was recorded on a 0.5 mM $^{13}C,^{15}N$ sample in 10% (vol/vol) D_2O with 1024 × 200 × 64 complex points and 12 ppm × 12 ppm × 43 ppm spectral widths in the observed ^{1}H × indirect $^{1}H \times ^{13}C$ dimensions. The joint composite-rotation adiabatic-sweep pulse sequence was used,[35] with τ_a of 4.8 ms and a longer mixing time ($\tau_{mix} = 200$ ms) to accentuate long distance interactions. WURST-20 adiabatic pulses[55] were used with an 80-kHz frequency sweep and τ_p of 2.1358 ms.[56] Where present, NOE cross-peaks to amide protons were used to confirm the protein assignment.

Paramagnetic lipid titrations

A single batch of purified KvAP VSD, after having been concentrated to 0.3 mM, was split into two equal samples. Paramagnetic 16-doxyl PSPC and diamagnetic PSPC lipids (Avanti Polar Lipids, Inc.), dissolved in chloroform, were aliquoted and dried under an argon stream. The dried lipid film was resuspended by the D7PC-solubilized KvAP VSD and incubated at room temperature for 30 min before data collection. Fast HSQC[57] spectra were acquired (at 18.8 T) using INEPT delays of 5.5 ms, a 3-9-19 WATERGATE pulse element,[58] and 512 × 150 complex points with 12.5 ppm × 25.6 ppm spectral widths in the $^{1}H \times ^{15}N$ dimensions. Lipid concentrations were limited to ≤2 mM to minimize simultaneous interactions with multiple paramagnetic agents, so that the paramagnetic relaxation enhancement is proportional to the bulk concentration of lipids. The relaxation enhancement ε was determined from single-exponential fits to the I_{doxyl}/I_{PSPC} peak intensity ratios using Curvefit[53] according to the relation $I_{doxyl}/I_{PSPC} = \exp(-\varepsilon c)$, where c is the concentration of lipids (see Hilty *et al.*[38]). Baseline noise was used as the uncertainty in peak intensity, and the error in ε was estimated using a Monte Carlo algorithm. Results from three samples (^{15}N, [^{15}N]GSRKF, and [^{15}N]GSAILV) were combined, and the average and standard error were used for residues with multiple data points.

Accession numbers

Chemical shift assignments have been deposited in the BioMagResBank under accession number 16957. Coordinates for the NMR ensemble of structures have been deposited in the Protein Data Bank under accession code 2KYH.

Acknowledgements

We thank the members of the MacKinnon laboratory for helpful suggestions throughout the course of this project, M. Whorton and A. Palmer for comments on the manuscript, and the staff at the New York Structural Biology Center for assistance with the spectrometers. The New York Structural Biology Center was supported by National Institutes of Health (NIH) grant P41 GM66354, and the 900-MHz spectrometers were purchased with funds from the NIH, the Keck Foundation, New York State, and the NYC Economic Development Corporation. This work was directly supported by NIH grant GM43939 (awarded to R.M). R.M. is an investigator of the Howard Hughes Medical Institute.

Supplementary Data

Supplementary data to this article can be found online at doi:10.1016/j.jmb.2010.09.012

References

1. Lee, S. Y., Letts, J. A. & Mackinnon, R. (2009). Functional reconstitution of purified human Hv1 H^+ channels. *J. Mol. Biol.* **387**, 1055–1060.

2. Tombola, F., Ulbrich, M. H. & Isacoff, E. Y. (2008). The voltage-gated proton channel Hv1 has two pores, each controlled by one voltage sensor. *Neuron*, **58**, 546–556.
3. Ramsey, I. S., Moran, M. M., Chong, J. A. & Clapham, D. E. (2006). A voltage-gated proton-selective channel lacking the pore domain. *Nature*, **440**, 1213–1216.
4. Sasaki, M., Takagi, M. & Okamura, Y. (2006). A voltage sensor-domain protein is a voltage-gated proton channel. *Science*, **312**, 589–592.
5. Hille, B. (2001). *Ion Channels of Excitable Membranes*, 3rd edit. Sinauer, Sunderland, MA.
6. Murata, Y., Iwasaki, H., Sasaki, M., Inaba, K. & Okamura, Y. (2005). Phosphoinositide phosphatase activity coupled to an intrinsic voltage sensor. *Nature*, **435**, 1239–1243.
7. Jiang, Y., Lee, A., Chen, J., Ruta, V., Cadene, M., Chait, B. T. & Mackinnon, R. (2003). X-ray structure of a voltage-dependent K^+ channel. *Nature*, **423**, 33–41.
8. Lee, S. Y., Lee, A., Chen, J. & Mackinnon, R. (2005). Structure of the KvAP voltage-dependent K^+ channel and its dependence on the lipid membrane. *Proc. Natl Acad. Sci. USA*, **102**, 15441–15446.
9. Long, S. B., Campbell, E. B. & Mackinnon, R. (2005). Voltage sensor of Kv1.2: structural basis of electromechanical coupling. *Science*, **309**, 903–908.
10. Long, S. B., Tao, X., Campbell, E. B. & Mackinnon, R. (2007). Atomic structure of a voltage-dependent K^+ channel in a lipid membrane-like environment. *Nature*, **450**, 376–382.
11. Schmidt, D., Cross, S. & Mackinnon, R. (2009). A gating model for the archeal voltage-dependent K^+ channel KvAP in DPhPC and POPE:POPG decane lipid bilayers. *J. Mol. Biol.* **390**, 902–912.
12. Ramu, Y., Xu, Y. & Lu, Z. (2006). Enzymatic activation of voltage-gated potassium channels. *Nature*, **442**, 696–699.
13. Schmidt, D. & Mackinnon, R. (2008). Voltage-dependent K^+ channel gating and voltage sensor toxin sensitivity depend on the mechanical state of the lipid membrane. *Proc. Natl Acad. Sci. USA*, **105**, 19275–19280.
14. Schmidt, D., Jiang, Q. X. & Mackinnon, R. (2006). Phospholipids and the origin of cationic gating charges in voltage sensors. *Nature*, **444**, 775–779.
15. Xu, Y., Ramu, Y. & Lu, Z. (2008). Removal of phospho-head groups of membrane lipids immobilizes voltage sensors of K^+ channels. *Nature*, **451**, 826–829.
16. Lee, S. Y. & Mackinnon, R. (2004). A membrane-access mechanism of ion channel inhibition by voltage sensor toxins from spider venom. *Nature*, **430**, 232–235.
17. Ruta, V. & Mackinnon, R. (2004). Localization of the voltage-sensor toxin receptor on KvAP. *Biochemistry*, **43**, 10071–10079.
18. Swartz, K. J. (2007). Tarantula toxins interacting with voltage sensors in potassium channels. *Toxicon*, **49**, 213–230.
19. Chakrapani, S., Cuello, L. G., Cortes, D. M. & Perozo, E. (2008). Structural dynamics of an isolated voltage-sensor domain in a lipid bilayer. *Structure*, **16**, 398–409.
20. Cuello, L. G., Cortes, D. M. & Perozo, E. (2004). Molecular architecture of the KvAP voltage-dependent K^+ channel in a lipid bilayer. *Science*, **306**, 491–495.
21. Shenkarev, Z. O., Paramonov, A. S., Lyukmanova, E. N., Shingarova, L. N., Yakimov, S. A., Dubinnyi, M. A. *et al.* (2010). NMR structural and dynamical investigation of the isolated voltage-sensing domain of the potassium channel KvAP: implications for voltage gating. *J. Am. Chem. Soc.* **132**, 5630–5637.
22. Cavanagh, J., Fairbrother, W. J., Palmer, A. G. & Skelton, N. J. (1996). *Protein NMR Spectroscopy: Principles and Practice.* Academic Press, San Diego, CA.
23. Tugarinov, V., Kanelis, V. & Kay, L. E. (2006). Isotope labeling strategies for the study of high-molecular-weight proteins by solution NMR spectroscopy. *Nat. Protoc.* **1**, 749–754.
24. Cornilescu, G., Delaglio, F. & Bax, A. (1999). Protein backbone angle restraints from searching a database for chemical shift and sequence homology. *J. Biomol. NMR*, **13**, 289–302.
25. Banerjee, A. & Mackinnon, R. (2008). Inferred motions of the S3a helix during voltage-dependent K^+ channel gating. *J. Mol. Biol.* **381**, 569–580.
26. Jiang, Y., Ruta, V., Chen, J., Lee, A. & Mackinnon, R. (2003). The principle of gating charge movement in a voltage-dependent K^+ channel. *Nature*, **423**, 42–48.
27. Ruta, V., Chen, J. & Mackinnon, R. (2005). Calibrated measurement of gating-charge arginine displacement in the KvAP voltage-dependent K^+ channel. *Cell*, **123**, 463–475.
28. Lee, S. Y., Banerjee, A. & Mackinnon, R. (2009). Two separate interfaces between the voltage sensor and pore are required for the function of voltage-dependent K^+ channels. *PLoS Biol.* **7**, e47.
29. Wang, C., Rance, M. & Palmer, A. G. (2003). Mapping chemical exchange in proteins with MW > 50 kD. *J. Am. Chem. Soc.* **125**, 8968–8969.
30. Hwang, P. M., Skrynnikov, N. R. & Kay, L. E. (2001). Domain orientation in beta-cyclodextrin-loaded maltose binding protein: diffusion anisotropy measurements confirm the results of a dipolar coupling study. *J. Biomol. NMR*, **20**, 83–88.
31. Shan, X., Gardner, K. H., Muhandiram, D. R., Rao, N. S., Arrowsmith, C. H. & Kay, L. E. (1996). Assignment of ^{15}N, $^{13}C^{\alpha}$, $^{13}C^{\beta}$, and H^N resonances in an ^{15}N, ^{13}C, ^{2}H labeled 64 kDa trp repressor–operator complex using triple-resonance NMR spectroscopy and ^{2}H-decoupling. *J. Am. Chem. Soc.* **118**, 6570–6579.
32. Fernández, C., Hilty, C., Wider, G. & Wüthrich, K. (2002). Lipid–protein interactions in DHPC micelles containing the integral membrane protein OmpX investigated by NMR spectroscopy. *Proc. Natl Acad. Sci. USA*, **99**, 13533–13537.
33. Liang, B., Arora, A. & Tamm, L. K. (2009). Fast-time scale dynamics of outer membrane protein A by extended model-free analysis of NMR relaxation data. *Biochim. Biophys. Acta*, **1798**, 68–76.
34. Hwang, P. M., Choy, W. Y., Lo, E. I., Chen, L., Forman-Kay, J. D., Raetz, C. R. H. *et al.* (2002). Solution structure and dynamics of the outer membrane enzyme PagP by NMR. *Proc. Natl Acad. Sci. USA*, **99**, 13560–13565.
35. Valentine, E. R., Ferrage, F., Massi, F., Cowburn, D. & Palmer, A. G. (2007). Joint composite-rotation adiabatic-sweep isotope filtration. *J. Biomol. NMR*, **38**, 11–22.
36. White, S. H. & Wimley, W. C. (1999). Membrane protein folding and stability: physical principles. *Annu. Rev. Biophys. Biomol. Struct.* **28**, 319–365.

37. Vogel, A., Scheidt, H. A. & Huster, D. (2003). The distribution of lipid attached spin probes in bilayers: application to membrane protein topology. *Biophys. J.* **85**, 1691–1701.
38. Hilty, C., Wider, G., Fernández, C. & Wüthrich, K. (2004). Membrane protein–lipid interactions in mixed micelles studied by NMR spectroscopy with the use of paramagnetic reagents. *ChemBioChem*, **5**, 467–473.
39. Jarvet, J., Danielsson, J., Damberg, P., Oleszczuk, M. & Gräslund, A. (2007). Positioning of the Alzheimer Aβ(1–40) peptide in SDS micelles using NMR and paramagnetic probes. *J. Biomol. NMR*, **39**, 63–72.
40. Jarvet, J., Zdunek, J., Damberg, P. & Gräslund, A. (1997). Three-dimensional structure and position of porcine motilin in sodium dodecyl sulfate micelles determined by ^{1}H NMR. *Biochemistry*, **36**, 8153–8163.
41. Swartz, K. J. (2008). Sensing voltage across lipid membranes. *Nature*, **456**, 891–897.
42. Clayton, G. M., Altieri, S., Heginbotham, L., Unger, V. M. & Morais-Cabral, J. H. (2008). Structure of the transmembrane regions of a bacterial cyclic nucleotide-regulated channel. *Proc. Natl Acad. Sci. USA*, **105**, 1511–1515.
43. Alabi, A. A., Bahamonde, M. I., Jung, H. J., Kim, J. I. & Swartz, K. J. (2007). Portability of paddle motif function and pharmacology in voltage sensors. *Nature*, **450**, 370–375.
44. Shenkarev, Z. O., Lyukmanova, E. N., Paramonov, A.S., Shingarova, L. N., Chupin, V. V., Kirpichnikov, M. P. *et al.* (2010). Lipid–protein nanodiscs as reference medium in detergent screening for high-resolution NMR studies of integral membrane proteins. *J. Am. Chem. Soc.* **132**, 5628–5629.
45. Delaglio, F., Grzesiek, S., Vuister, G. W., Zhu, G., Pfeifer, J. & Bax, A. (1995). NMRPipe: a multidimensional spectral processing system based on UNIX pipes. *J. Biomol. NMR*, **6**, 277–293.
46. Goddard, T. D. & Kneller, D. G. (2003). *SPARKY 3.* University of California, San Francisco, CA.
47. Loria, J. P., Rance, M. & Palmer, A. G. (1999). Transverse-relaxation-optimized (TROSY) gradient-enhanced triple-resonance NMR spectroscopy. *J. Magn. Reson.* **141**, 180–184.
48. Neri, D., Szyperski, T., Otting, G., Senn, H. & Wüthrich, K. (1989). Stereospecific nuclear magnetic resonance assignments of the methyl groups of valine and leucine in the DNA-binding domain of the 434 repressor by biosynthetically directed fractional ^{13}C labeling. *Biochemistry*, **28**, 7510–7516.
49. Schwieters, C., Kuszewski, J. & Marius Clore, G. (2006). Using Xplor-NIH for NMR molecular structure determination. *Prog. Nucl. Magn. Reson. Spectrosc.* **48**, 47–62.
50. Schwieters, C. D., Kuszewski, J. J., Tjandra, N. & Clore, G. M. (2003). The Xplor-NIH NMR molecular structure determination package. *J. Magn. Reson.* **160**, 65–73.
51. Kuszewski, J., Gronenborn, A. M. & Clore, G. M. (1997). Improvements and extensions in the conformational database potential for the refinement of NMR and X-ray structures of proteins and nucleic acids. *J. Magn. Reson.* **125**, 171–177.
52. Grishaev, A. & Bax, A. (2004). An empirical backbone–backbone hydrogen-bonding potential in proteins and its applications to NMR structure refinement and validation. *J. Am. Chem. Soc.* **126**, 7281–7292.
53. Palmer, A. G. (www.palmer.hs.columbia.edu).
54. Tjandra, N., Feller, S., Pastor, R. & Bax, A. (1995). Rotational diffusion anisotropy of human ubiquitin from ^{15}N NMR relaxation. *J. Am. Chem. Soc.* **117**, 12562–12566.
55. Kupce, E. & Freeman, R. (1995). Adiabatic pulses for wide-band inversion and broad-band decoupling. *J. Magn. Reson. Ser. A*, **115**, 273–276.
56. Zwahlen, C., Legault, P., Vincent, S., Greenblatt, J., Konrat, R. & Kay, L. (1997). Methods for measurement of intermolecular NOEs by multinuclear NMR spectroscopy: application to a bacteriophage lambda N-peptide/boxB RNA complex. *J. Am. Chem. Soc.* **119**, 6711–6721.
57. Mori, S., Abeygunawardana, C., Johnson, M. O. & van Zijl, P. C. (1995). Improved sensitivity of HSQC spectra of exchanging protons at short interscan delays using a new fast HSQC (FHSQC) detection scheme that avoids water saturation. *J. Magn. Reson. Ser. B*, **108**, 94–98.
58. Sklenar, V., Piotto, M., Leppik, R. & Saudek, V. (1993). Gradient-tailored water suppression for ^{1}H–^{15}N HSQC experiments optimized to retain full sensitivity. *J. Magn. Reson. Ser. A*, **102**, 241–245.
59. Venters, R. A., Farmer, B. T., Fierke, C. A. & Spicer, L.D. (1996). Characterizing the use of perdeuteration in NMR studies of large proteins: ^{13}C, ^{15}N and ^{1}H assignments of human carbonic anhydrase II. *J. Mol. Biol.* **264**, 1101–1116.
60. Wishart, D. S. & Case, D. A. (2001). Use of chemical shifts in macromolecular structure determination. *Methods Enzymol.* **338**, 3–34.
61. The PyMOL Molecular Graphics System, Schrödinger, LLC (www.pymol.org).